RSC Advances

ROYAL SOCIETY OF CHEMISTRY

PAPER

View Article Online
View Journal | View Issue

Check for updates

Cite this: *RSC Adv.*, 2025, **15**, 23489

First-principles calculations of the photocatalytic performance of ZnO–MX_2 (M = Mo, W; X = S, Se) heterojunctions

Meng-Yao Dai,[ab] Xue Wen,[ab] Rui Xia,[ab] Yi-Min Zheng,[ab] Lai Wei,[ab] Li-Li Zhang,*[ab] Xiao-Hui Liang[c] and Yi-Neng Huang*[ad]

In this work, we systematically investigate the stability, electronic structure, optical properties, and photocatalytic performance of four ZnO–MX_2 (M = Mo, W; X = S, Se) heterojunctions. The results indicate that all four heterojunctions exhibit excellent structural stability. In each system, an internal electric field is formed from the ZnO layer to the MX_2 layer, facilitating the effective transfer of electrons. Moreover, the effective mass of holes in these systems is greater than that of electrons, suggesting efficient separation of electron–hole pairs, which enhances photocatalytic efficiency. Compared with monolayer ZnO, the band gap of the heterojunctions is significantly reduced, and all heterojunctions display direct band gap characteristics. Simultaneously, the static dielectric constant of these systems increases, and redshift is observed in their absorption spectra. Both ZnO–$MoSe_2$ and ZnO–WSe_2 exhibit type I band alignment, making them unsuitable for photocatalytic applications but ideal candidates for solar cells. On the other hand, ZnO–MoS_2 and ZnO–WS_2 exhibit a II-type band alignment. In comparison to ZnO–MSe_2, they demonstrate a higher static dielectric constant and light absorption coefficient, as well as a larger *D* value (the ratio of the effective mass of electrons to holes), which suggests their superior photocatalytic efficiency. Notably, while ZnO–MoS_2 only possesses hydrogen evolution reaction (HER) capability, ZnO–WS_2 demonstrates both HER and oxygen evolution reaction (OER) capabilities.

Received 7th May 2025
Accepted 26th June 2025

DOI: 10.1039/d5ra03215f

rsc.li/rsc-advances

1. Introduction

Since the end of the 20th century, with the acceleration of industrialization and the continuous growth of the global population, energy shortages and environmental pollution have gradually become key challenges restricting the sustainable development of society.[1,2] The rise of photocatalytic technology has provided a brand-new approach for effectively utilizing solar energy to address resource scarcity and ecological crises.[3] In recent years, researchers have been dedicated to developing high-performance photocatalysts and applying them in multiple fields such as hydrogen production,[4] pollutant degradation,[5] microbial inactivation,[6] and artificial photosynthesis simulation,[7] with the aim of achieving the dual goals of environmental governance and clean energy production. However, the development of efficient photocatalysts is still limited by factors such as rapid recombination of photogenerated carriers and insufficient active sites. Two-dimensional materials,[8] with their unique advantages such as high specific surface area, ultrafast carrier mobility, and abundant interfacial active sites, have shown excellent application potential in the field of photocatalysis. Compared with three-dimensional ZnO, experimental studies have shown that monolayer ZnO, due to its larger specific surface area, experiences carrier migration that leads to an increase in effective mass and a decrease in mobility. However, the exciton binding energy significantly increases, thereby causing a reduction in the band gap. Therefore, it shows broad application prospects in the field of two-dimensional optoelectronic devices and beyond. Two-dimensional ZnO, with its vertically stacked structure similar to graphene and a high surface area-to-volume ratio, exhibits outstanding optoelectronic properties, such as superior optical transparency, enhanced carrier mobility, and efficient light absorption capacity.[9] In addition, its tunable bandgap structure further enhances its adaptability in optoelectronic applications. However, the practical application of ZnO monolayers is still constrained by some inherent limitations: (1) chemical degradation is prone to occur in harsh environments such as high temperature, high humidity, or corrosive media;[10] (2) the

---

[a] *Xinjiang Laboratory of Phase Transitions and Microstructures in Condensed Matters, College of Physical Science and Technology, Yili Normal University, Yining 835000, China. E-mail: suyi2046@sina.com*

[b] *Yili Engineering Research Center of Green Silicon-Based Materials, Yining, Xinjiang, 83500, China*

[c] *Hangzhou Dianzi University, Hangzhou, 310018, People's Republic of China*

[d] *National Laboratory of Solid State Microstructures, College of Physics, Nanjing University, Nanjing 210093, China. E-mail: ynhuang@nju.edu.cn*

relatively large bandgap (about 3.37 eV) leads to a fast electron–hole recombination rate, thereby limiting the improvement of carrier mobility;[11] (3) due to the rigid band structure characteristics, the flexibility in modulating optical properties is rather limited.[12]

In response to the above challenges, in recent years, the strategy of constructing vertical heterostructures based on ZnO has received extensive attention.[13,14] Haddad *et al.*[15] synthesized CuO/ZnO heterojunctions with different CuO contents *via* a low-temperature coprecipitation method. Photocatalytic characterization indicated that they were p-type semiconductors with holes as the dominant carriers, demonstrating excellent photocatalytic performance. The conduction band potential of CuO was more negative than that of ZnO, which facilitated the electron transfer for adsorbed water oxidation and hydrogen generation. Among them, the sample with a 5% CuO doping ratio exhibited the best photocatalytic activity. Li *et al.*[16] prepared CeO_2/ZnO heterostructures *via in situ* hydrothermal synthesis. This heterostructure effectively promoted the separation of photogenerated electron–hole pairs, significantly reduced the charge recombination rate, and modulated the electronic properties of the material. At the same time, it enhanced the surface adsorption capacity for oxygen molecules, thereby promoting the generation of superoxide radicals (O_2^-), and ultimately significantly improved the photocatalytic performance. Yuan *et al.*[17] prepared ZnO/GaN(O) heterojunctions by an *in situ* re-oxidation method and significantly enhanced the separation efficiency of hot carriers, effectively delayed the electron–hole pair recombination process by optimizing the heterostructure and microstructure, thereby improving the adsorption and activation performance of NO. These studies jointly promoted the application and development of ZnO-based heterostructures in the field of photocatalysis. In terms of experimental research, Jia *et al.*[18] successfully synthesized MoS_2/ZnO heterojunctions using nano-photothermal energy-driven technology. The research results show that, compared with single-layer materials, this heterojunction exhibits more excellent optical properties. In addition, by real-time regulation of the laser wavelength, processing time, and power parameters, a simple and precise *in situ* control preparation process for new functional materials can be achieved. Jiang *et al.*[19] successfully fabricated WS_2, ZnO thin films and ZnO & WS_2 (ZnO@WS_2 and WS_2@ZnO) heterojunction composite films through single-step or two-step radio frequency magnetron sputtering. The research indicates that the optical absorption performance of the ZnO@WS_2 heterojunction composite film is significantly superior to that of the single-layer films, and its carrier lifetime is notably longer than that of the WS_2 film, demonstrating promising application prospects in the field of nonlinear optical materials. In addition, theoretical computational research can effectively make up for the deficiency of experimental research in exploring microscopic mechanisms and provide reasonable microscopic explanations for the macroscopic phenomena observed in experiments. In theoretical calculations, Guan *et al.*[20] designed a novel ZnO/$MoSe_2$ van der Waals heterostructure with a bandgap of 1.556 eV. Research shows that under photoexcitation conditions, electrons can efficiently migrate from the conduction band of the ZnO monolayer to that of the $MoSe_2$ monolayer, thereby achieving efficient carrier separation. This band alignment not only helps enhance the absorption capacity of visible light but also significantly promotes the effective excitation of carriers. Wang *et al.*[21] fabricated ZnO/MoS_2 and ZnO/$MoSe_2$ composites and compared them with the individual monolayer systems. The study demonstrated that electrons transferred from the ZnO side to the MoS_2 ($MoSe_2$) side, a feature that effectively promotes the separation and transport of photogenerated carriers, thereby significantly enhancing the photocatalytic efficiency. Additionally, the absorption edge of the composites shifted significantly towards the visible light region compared to pure ZnO and MoX_2 monolayers, indicating their potential for important applications as photocatalysts in water splitting.

Experimentally, the three heterojunctions of ZnO/WS_2, ZnO/$MoSe_2$, and ZnO/MoS_2 have been individually studied after synthesis; theoretically, only comparative studies of ZnO/MoS_2 and ZnO/$MoSe_2$ have been conducted, while collectively comparative studies on the theoretical mechanisms of the four ZnO/MX_2 heterojunctions are rarely reported. The electron transfer mechanism plays a crucial role in the photocatalytic process, directly determining the separation efficiency of photogenerated carriers, the selectivity of reaction pathways, and the overall catalytic performance. Therefore, this study adopted the first-principles method to systematically calculate and deeply explore the stability, electronic structure, optical properties and photocatalytic performance of ZnO–MX_2 ($M = Mo, W$; $X = S, Se$) materials, and further revealed the intrinsic mechanism for the differences in photocatalytic efficiency among this series of heterojunctions. This research not only provides important theoretical guidance for the design of efficient photocatalytic materials, but also lays a solid theoretical foundation for the development of new materials with higher photocatalytic activity.

2. Computational methods and model construction

2.1 Calculation method

All the calculations in this paper are based on Density Functional Theory (DFT) and the Projector-Augmented-Wave (PAW) method,[22] and were carried out using the VASP (Vienna *Ab initio* Simulation Package)[23] software package. To obtain accurate calculation results, the cutoff energy is set to 520 eV, the self-consistent field (SCF) convergence accuracy is 2×10^{-6} eV per atom, and the *k*-points in the first Brillouin zone are sampled using a 3 × 3 × 1 Monkhorst–Pack grid. To avoid the interaction between adjacent supercells along the interlayer, a vacuum layer of 18 Å was added in the out-of-plane vertical direction for the four groups of heterojunction structures. Geometric optimization was carried out using the BFGS algorithm, and van der Waals forces were taken into account with the Tkatchenko–Scheffler (TS) dispersion correction.[24] All calculations were performed in reciprocal lattice vector space. In addition, the stability of the heterojunction system was tested using the *ab initio* molecular dynamics (AIMD). The AIMD test based on DFT used the Nosé–Hoover thermostat to control the temperature, with a total simulation length of 8000 steps and a time step of 0.8 fs.

2.2 Model construction

This paper studies the relatively stable ideal ZnO crystal, whose stable phase is hexagonal wurtzite and belongs to the $P6_3mc$ space group, with unit cell parameters of $\alpha = \beta = 90°$ and $\gamma = 120°$. The chalcogenide compounds MoS_2 and $MoSe_2$ belong to the $P6_3/mmc$ space group, and the stable phase of these two structures is the 2H phase, which exhibits semiconductor properties. The 2H phase adopts an ABA stacking mode, that is, the sulfur atoms in the upper layer are directly above those in the lower layer. WS_2 and WSe_2 are characterized by the periodic arrangement of metal and chalcogen elements in a hexagonal structure. However, this hexagonal structure differs from that of graphene. When observed along the *c*-axis, the structural arrangement in the system forms an *X*–*M*–*X* sandwich.

The ZnO unit cell was expanded by 3 × 3 × 1, and a single layer was cut along the (001) plane. The optimized model is shown in Fig. 1(a). The band structure of the single-layer ZnO was calculated using both the Perdew–Burke–Ernzerhof (PBE)[25] functional and the hybrid functional Heyd–Scuseria–Ernzerhof (HSE06).[26] The band gap calculated using the HSE06 hybrid functional is 3.32 eV (as shown in Fig. 1(a)), and the error compared to the experimental results is only 0.602%.[27] This value is closer to the actual result than that obtained using PBE (as shown in Fig. 1(b)). Consequently, all subsequent calculations in this work will employ the HSE06 method. According to Fig. 2, the optimal interlayer distances of ZnO–MX_2 are 3.401 Å, 2.966 Å, 3.302 Å, and 2.808 Å, respectively.

3. Analysis and discussion

3.1 Stability analysis

3.1.1 Lattice mismatch rate and binding energy. To form a stable heterojunction, the two materials should have crystal structures as similar or consistent as possible, and the lattice mismatch rate (σ) between the two types of materials should be less than 5%.[28] This paper calculates the σ of four types of heterojunctions. Then, σ of these four systems is defined as follows:[29]

$$\sigma = (a_2 - a_1)/a_1 \tag{1}$$

Here, a_1 denotes the lattice constant of the single-layer ZnO supercell, while a_2 denotes the lattice constant of the MX_2 supercell. After geometric optimization, the optimal model of the heterojunction was obtained. According to the above formula, the σ of these four heterostructures were calculated and are shown in Table 1. All the σ values are less than 5%, which indicates that all four heterojunctions can be successfully constructed.

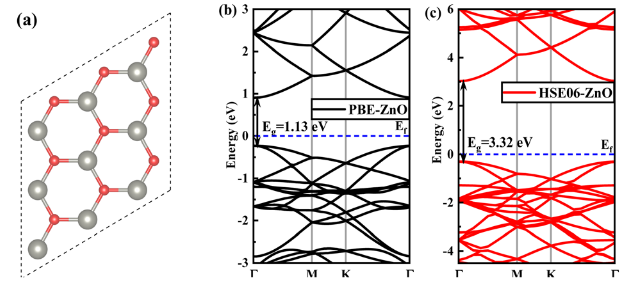

Fig. 1 (a) Crystal model of single-layer ZnO; (b) band structure calculated by PBE; and (c) band structure calculated by HSE06.

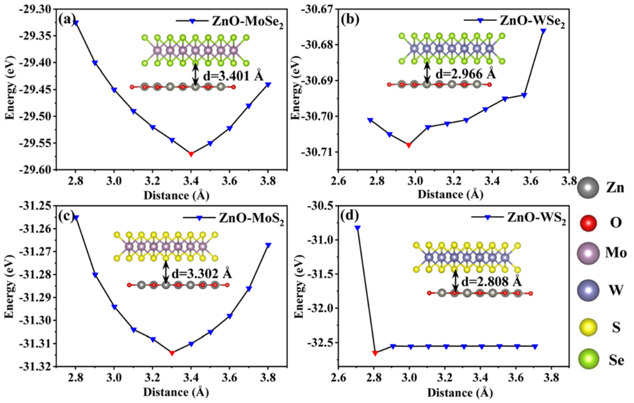

Fig. 2 Layer spacing optimization test diagram (a) ZnO–$MoSe_2$ (b) ZnO–WSe_2 (c) ZnO–MoS_2 (d) ZnO–WS_2.

To further discuss the structural stability, the binding energy of ZnO–MX_2 was also calculated. When E_b is negative, the larger its absolute value, the higher the stability of the system. The interface binding energy can be expressed as follows:[30]

$$E_b = E_{ZnO\text{–}MX_2} - E_{ZnO} - E_{MX_2} \tag{2}$$

where $E_{ZnO\text{–}MX_2}$ represents the total energy of the heterojunction, E_{ZnO} represents the energy of the single-layer ZnO, and E_{MX_2} represents the energy of MX_2 (M = Mo, W; X = S, Se). By calculating the binding energy, it can be determined that the binding energy of all systems is negative, indicating that these systems are stable. Among them, the binding energy value of ZnO–$MoSe_2$ is the smallest, indicating that this system is the most stable among the four heterojunctions.

3.1.2 AIMD test. To further evaluate the stability of ZnO–MX_2, this study continues to employ AIMD simulations to

Table 1 Layer spacing *d*, mismatch rate σ, binding energy E_b, and band gap width calculated by PBE and HSE06 of the ZnO–MX_2

Heterojunction	ZnO–$MoSe_2$	ZnO–WSe_2	ZnO–MoS_2	ZnO–WS_2
d (Å)	3.401	2.966	3.302	2.088
σ (%)	2.11	1.01	2.17	2.12
E_b (eV)	−7.20	−7.56	−6.99	−6.94
E_g (eV) PBE	1.129	1.421	0.235	1.420
E_g (eV) HSE06	1.956	2.098	1.014	1.493

calculate the thermodynamic stability of the four types of heterojunctions.[31] AIMD combines first-principles DFT with molecular dynamics (MD) techniques, enabling the determination of molecular motion within the DFT framework. As shown in Fig. 3, with the temperature set at 300 K, after 8000 steps of calculation within 0.8 fs, the system remains stable. As shown in Fig. 3, all four systems exhibit only minor structural changes, accompanied by negligible energy fluctuations, while the overall structure remains intact (see the illustrations). These results indicate that the four heterojunctions possess good thermodynamic stability at 300 K.

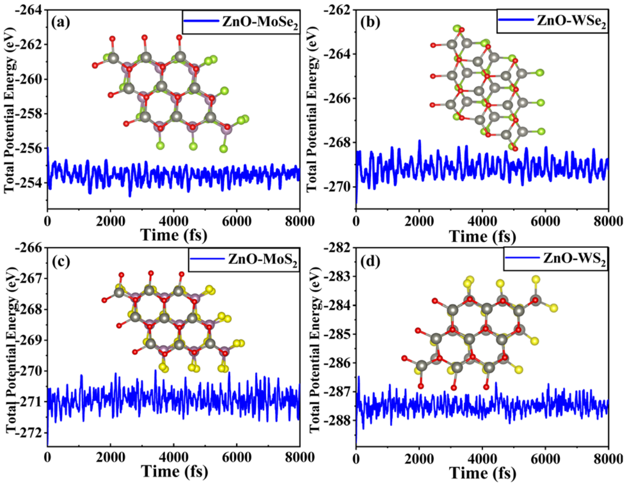

Fig. 3 AIMD curves of total energy and temperature of (a) ZnO–MoSe$_2$ (b) ZnO–WSe$_2$ (c) ZnO–MoS$_2$ (d) ZnO–WS$_2$ (the inset shows the top views of the four heterojunctions).

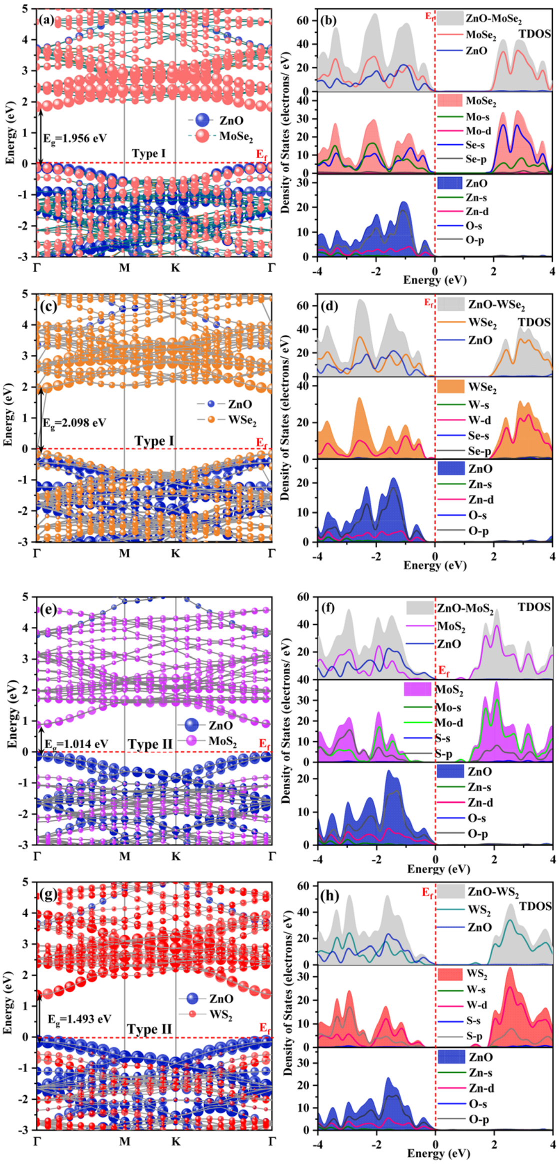

Fig. 4 (a and b) Show the band structure (left) and density of states (right) of ZnO–MoSe$_2$, (c and d) of ZnO–WSe$_2$, (e and f) of ZnO–MoS$_2$, and (g and h) of ZnO–WS$_2$. (In the figure, the contribution of each atom is represented by the size of the small balls. The larger the ball, the greater the contribution of the corresponding atom.)

3.2 Electronic structure

3.2.1 Band structure and electronic density of states.

To explore the electronic structures of the above four heterojunctions, the band structures and electronic density of states of ZnO–MX$_2$ were further calculated. In this study, the Fermi level was set as the energy zero point, and the band structures, total density of states (TDOS), and partial density of states (PDOS) near the Fermi level were primarily investigated. Fig. 4(a) and (b) respectively show the band structure and electronic density of states of the ZnO–MoSe$_2$. The band gap of this system is 1.956 eV, and it belongs to the direct transition type. Since indirect transitions will cause relaxation and energy loss during the electron transition process, the transition probability is relatively low. In addition to requiring photon energy, indirect transitions also need momentum exchange. In contrast, the direct transition process can avoid these drawbacks. It does not require phonon participation and only needs electrons to absorb photons of a certain energy to achieve electron transfer, thereby significantly improving the photocatalytic efficiency of the system. From the TDOS (see Fig. 4(b)), both the CBM and VBM are contributed by MoSe$_2$, indicating that it belongs to type I band alignment. By comparing the vertical coordinates of the total density of states diagrams of the four heterojunctions, it is found that the peak of the ZnO–MoSe$_2$ is the highest, indicating that there is a greater distribution of electrons in a specific energy range, that is, this system has a larger electronic density of states. This creates favorable conditions for electron transition, thereby enhancing electron mobility and is expected to significantly improve the photocatalytic efficiency of this system. From the analysis of the PDOS, it can be seen that the CBM is primarily provided by the Mo-4d states in the MoSe$_2$ layer, with contributions from the Se-4p and Se-4s states; the VBM is mainly contributed by the Mo-4d and Se-4p states in MoSe$_2$, while the O-2p states in ZnO also provide a significant contribution. Research findings indicate that type I band alignment is conducive to the recombination of photogenerated carriers. Although it is not suitable for application in the field of photocatalysis, it holds great potential for use in the field of luminescence, such as in light-emitting diodes (LEDs).

Fig. 4(c) and (d) respectively show the band structure and electron density diagram of ZnO–WSe_2, with a band gap of 2.098 eV. Compared to bulk ZnO, the band gap of this system is reduced; the conduction band position is significantly lowered, and the energy levels are more densely packed. It is a direct transition type. Electrons require less energy to transition from the top of the valence band to the bottom of the conduction band, leading to a redshift in the absorption edge and a significant enhancement in the response to visible light. From the analysis of the TDOS diagram, it can be seen that the CBM and VBM of this system are both contributed by WSe_2, indicating a type I band alignment. Under light irradiation, the photogenerated electron–hole pairs tend to accumulate in the WSe_2 layer, making effective separation challenging. The analysis of the DOS in the valence band and conduction band indicates that the CBM of the ZnO–WSe_2 is primarily composed of the W-5d states in WSe_2, while the VBM is mainly contributed by the O-2p states in ZnO and the W-5d states in WSe_2, with a minor contribution from the Zn-3d states in ZnO. In addition, a new peak emerged on the right side of the Fermi level, mainly contributed by the N-2p state, indicating that some energy levels split. This is manifested as a sparser energy level distribution in the band diagram. At 5.25 eV, the electronic orbitals of WSe_2 and ZnO overlap, which is conducive to electron transfer.

It can be seen from Fig. 4(e) and (f) that the band gap of ZnO–MoS_2 is 1.014 eV, and the transition mode is direct. The conduction band as a whole shifts downward, and the energy levels become more densely packed, indicating that the number of electrons that can be accommodated in this energy region increases, that is, the electron density in the system increases, leading to a higher transition probability and significantly improved photocatalytic efficiency. Furthermore, the CBM of this system is contributed by the MoS_2, while the VBM is contributed by the ZnO, indicating that it belongs to a type II heterojunction. From the TDOS diagram analysis, it is evident that MoS_2 plays a decisive role in determining the CBM and VBM. From the partial wave density of states analysis, it can be seen that the CBM of this system is primarily contributed by the Mo-4d and S-3p states in MoS_2, while the VBM is mainly composed of the Mo-4d and S-3p states in MoS_2 as well as the O-2p states in ZnO. The Mo-4d and S-3p electron orbitals fully overlap, and the electrons between different layers hybridize, thereby generating an internal electric field within the system that facilitates the transition of photogenerated carriers, thus improving both the injection efficiency and the charge flow rate. The above analysis indicates that the photocatalytic performance of this system has been significantly improved.

Fig. 4(g) and (h) respectively show the band structure and electronic density of states of the ZnO–WS_2. The band gap of this system is 1.493 eV. Compared with the single-layer ZnO (see Fig. 1(b)), the conduction band position shifts downward, the band gap narrows, and the energy levels become more dense, indicating a direct transition type. Its CBM is mainly contributed by the WS_2, while the VBM is mainly contributed by the ZnO, which belongs to the type II band alignment. From the DOS diagram analysis, it can be seen that the conduction band is primarily contributed by WS_2, while the valence band is jointly composed of ZnO and WS_2. The wave function-resolved DOS analysis indicates that the VBM of the ZnO–WS_2 is mainly provided by the W-5d state in WS_2 and the O-2p state in ZnO, with minor contributions from the W-6s state in WS_2 and the Zn-4s state in ZnO; meanwhile, the CBM is predominantly provided by the W-5d state in WS_2. The CBM of this system originates from WS_2, and the VBM originates from ZnO, forming a type II heterojunction, which is consistent with the band structure diagram. This process significantly enhances electron migration efficiency, thereby effectively boosting the photocatalytic activity of the entire system.

Overall, the ZnO–$MoSe_2$ and ZnO–WSe_2 are type I heterojunctions. The photogenerated electrons transfer from the CBM of ZnO to the CBM of $MoSe_2$ and WSe_2. This band structure is conducive to the rapid recombination of photogenerated carriers, and thus is mainly applied in the field of light-emitting devices such as LEDs and photovoltaic cells. Meanwhile, ZnO–MoS_2 and ZnO–WS_2 belong to type II heterojunctions, with their energy bands arranged in an offset manner. This causes the photogenerated electrons and holes to accumulate in different materials, respectively, effectively suppressing the recombination of photogenerated carriers and promoting carrier separation. This type of heterojunction is mainly applied in fields such as photocatalysis and photodetection. For instance, in the process of photocatalytic water splitting for hydrogen production, it can significantly enhance the separation efficiency of photogenerated electron–hole pairs, thereby increasing the overall efficiency of the photocatalytic reaction.

3.2.2 Work function and differential charge density. To deeply explore the distribution characteristics of electrons in the internal regions of heterojunctions, this paper calculates their differential charge density. Fig. 5(a)–(d) present the planar average electrostatic potential curves and three-dimensional

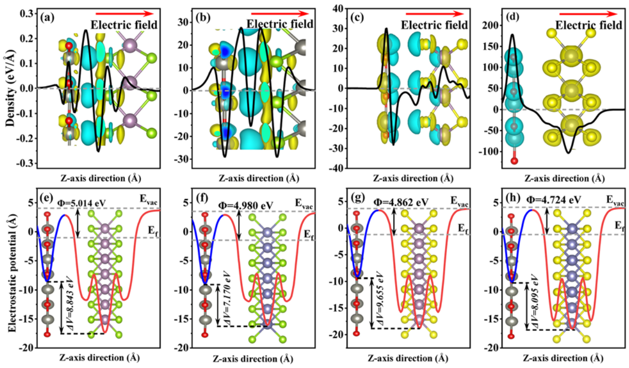

Fig. 5 Presents the planar average electrostatic potential diagrams of (a) ZnO–$MoSe_2$, (b) ZnO–WSe_2, (c) ZnO–MoS_2, and (d) ZnO–WS_2. The inset figures illustrate the side views of the three-dimensional differential charge density (yellow indicates electron accumulation, while cyan indicates depletion). Panels (e) ZnO–$MoSe_2$, (f) ZnO–WSe_2, (g) ZnO–MoS_2, and (h) ZnO–WS_2 depict the work function diagrams, with the inset figures showing the side views of the corresponding single-layer system models.

differential charge density diagrams for four groups of heterojunctions. The calculation expression is:[32]

$$\Delta\rho = \rho_{(\mathrm{ZnO/MX_2})} - \rho_{(\mathrm{ZnO})} - \rho_{(\mathrm{MX_2})} \quad (3)$$

Among them, $\rho_{(\mathrm{ZnO/MX_2})}$ represents the charge density of the four heterojunction systems, $\rho_{(\mathrm{ZnO})}$ represents the charge density of the ZnO layer, and $\rho_{(\mathrm{MX_2})}$ represents the charge density of the MX_2 layer. Research has found that there is an interaction force between the two layers of semiconductor materials that make up a heterojunction, causing a redistribution of charges and thus forming an internal electric field at their interface. When the heterojunction is illuminated, photons interact with the electrons in the semiconductor materials, generating photogenerated electron–hole pairs. Under the influence of the internal electric field, these photogenerated electrons undergo directed movement, leading to efficient separation of the photogenerated electron–hole pairs. In the three-dimensional differential charge density diagram, cyan indicates electron depletion and yellow indicates electron accumulation. It can be seen that the electrons in the four groups of heterojunctions all migrate from the MX_2 to the ZnO, and the direction of the built-in electric field points from the ZnO to the MX_2. This process helps to efficiently separate the photogenerated electron–hole pairs, enabling more electrons and holes to participate in the redox reaction, thereby significantly enhancing the photocatalytic activity of the system. The analysis of the planar average electrostatic potential curve shows that positive values indicate electron depletion, while negative values suggest electron accumulation. In the four systems, electrons are depleted in the MX_2 and accumulated in the ZnO, indicating electron migration from the MX_2 layer to the ZnO, which is consistent with the results of the three-dimensional image. The work function refers to the minimum energy required to transfer an electron from the interior of a semiconductor to its surface. It reflects the strength of the material's binding ability to electrons; that is, the larger the work function, the greater the difficulty for electrons to escape from the material, and the stronger the binding ability to electrons; conversely, the smaller the work function, the easier it is for electrons to escape. In this paper, the work functions of four groups of heterojunctions were further calculated, and the expression is:[33]

$$\Phi = E_{\mathrm{vac}} - E_{\mathrm{Fermi}} \quad (4)$$

where, E_{vac} represents the vacuum level, and E_{Fermi} represents the Fermi level. The difference between the two is the work function (Φ), as shown in Fig. 5(e)–(h). The work functions of the ZnO–MX_2 are 5.014 eV, 4.980 eV, 4.862 eV, and 4.724 eV, respectively. Moreover, all four systems exhibit a significant potential difference, which can effectively separate photogenerated carriers. It can be seen from the figure that the photogenerated electrons migrate from the MX_2 with a lower potential to the ZnO with a higher potential until the Fermi levels of both reach equilibrium. The direction of the built-in electric field points from the ZnO to the MX_2, which is consistent with the calculation results of the differential charge density. In addition, due to the existence of the built-in electric field, the separation of photogenerated carriers is effectively promoted, thereby significantly suppressing their recombination. Therefore, more electrons and holes can participate in the photocatalytic reaction process, greatly enhancing the photocatalytic efficiency of the heterojunction system.

3.2.3 Effective mass. In the process of solar water splitting, the recombination of electrons and holes after absorbing sunlight is also a key factor in achieving the photocatalytic process. We calculated the effective masses of electrons (m_e^*) and holes (m_h^*) in the ZnO–MX_2 as well as their ratio (D) to evaluate the retention of electrons and holes in the system after absorbing light. The formula for effective mass is given by:[34]

$$m^* = \hbar^2 \Big/ \left(\frac{\partial^2 E}{\partial K^2}\right) \quad (5)$$

The unit of $(\partial^2 E/\partial K^2)$ is $(2\pi/a)^2$ eV, where $\hbar = h/2\pi$. A higher D value indicates a greater difference in the effective masses of electrons and holes in the system. Although D is not a direct criterion for the recombination rate, it provides a way to determine whether the photogenerated electrons and holes can be utilized in the photocatalytic water splitting process. As shown in Table 2, the effective mass of holes in all systems is greater than that of electrons, forming a heavy-hole–light-electron system. This further suggests that electrons and holes within the system can be effectively separated.

The effective electron mass (m_e^*) of the ZnO–MoS_2 is slightly larger than that of monolayer ZnO due to the contribution of the S-3s state in the conduction band. Compared with monolayer ZnO, the effective hole mass in the heterojunction system has increased. In the ZnO–WSe_2, the D value is closest to 1, indicating that the electron and hole mobilities are not significantly different. This suggests that this system may not be very suitable for use as a photocatalyst. Compared with the literature, the errors in the effective masses of electrons and holes calculated in this paper are 5% and 4%, respectively, indicating that the calculation results of this paper have reference value.[35] Compared with ZnO, the D value of the ZnO–MX_2 significantly increases, indicating that after constructing the heterojunction, the recombination rate of photogenerated electrons and holes in the system decreases, thereby effectively enhancing the photocatalytic efficiency of the material. Among them, the D value of the ZnO–WS_2 is the highest, meaning that the separation of electrons and holes in this system is most pronounced, making it less likely for them to recombine and facilitating further separation of photogenerated carriers.

Table 2 Optimized effective mass m^* (m_0) (Å) and D of ZnO–MX_2

Systems	ZnO	ZnO–$MoSe_2$	ZnO–WSe_2	ZnO–MoS_2	ZnO–WS_2
m_e^*	0.31	0.32	0.36	0.27	0.31
m_h^*	0.19	0.40	0.43	0.36	0.48
D (m_h^*/m_e^*)	0.61	1.25	1.13	1.33	1.55

The *D* values of ZnO–MS$_2$ are greater than those of ZnO–MSe$_2$, suggesting a more prominent separation of electrons and holes in ZnO–MS$_2$. This phenomenon reduces the probability of carrier recombination and promotes the further separation of photogenerated carriers. This finding is consistent with the characteristic of ZnO–MS$_2$ forming a type-II heterojunction, which effectively enhances the separation of electron–hole pairs.

3.3 Optical properties

The magnitude of the dielectric function reflects the strength of a medium's ability to bind charges. The larger the magnitude of the dielectric function, the stronger the material's response to an electric field and the greater its polarization capacity. From the real part of the dielectric function graph in Fig. 6(a), it can be seen that the static dielectric constants of the five systems, ZnO, ZnO–MoSe$_2$, ZnO–WSe$_2$, ZnO–MoS$_2$, and ZnO–WS$_2$, are 2.32, 1.77, 4.93, 1.98, and 5.72, respectively. By comparison, it can be seen that the static dielectric constant value of the ZnO–WS$_2$ is the largest, indicating a higher number of electric dipoles in this system, which can maximize the carrier density and the efficiency of charge transport and separation. In the visible light range around 2 eV, both the ZnO–WS$_2$ and ZnO–WSe$_2$ exhibit a prominent and sharp peak, indicating that these two heterojunctions have a stronger response to light and a greater polarization capacity.

As shown in Fig. 6(b), the absorption edge of ZnO is approximately at 430 nm, and its light absorption intensity gradually decreases within the range of 450 to 800 nm, with almost no obvious absorption peak. The absorption peaks of the four heterojunctions are all significantly higher than that of ZnO, with the absorption band edges redshifted and shifted towards the low-energy region. The intensity of light absorption shows an upward trend. At approximately 5.32 eV, the light absorption peaks of the four systems overlap, indicating that the light absorption intensity reaches its maximum at this energy level.

The above results are due to the fact that, compared to the ZnO$_2$ monolayer, the band gaps of all heterojunctions exhibit a decreasing trend, which correspondingly reduces the minimum photon energy required for electron transitions. This enables the material to absorb photons with longer wavelengths (*i.e.*, lower energy) – for example, extending the absorption range from ultraviolet light to visible light or even infrared light – thereby effectively broadening the spectral range of light absorption. Additionally, the built-in electric field present in the heterojunction accelerates the transition process of photogenerated electrons through the action of the electric field force. Therefore, under the synergistic effect of the reduced band gap and the built-in electric field, the absorption coefficients of all four systems are significantly enhanced, and their absorption spectra all exhibit redshift phenomena.

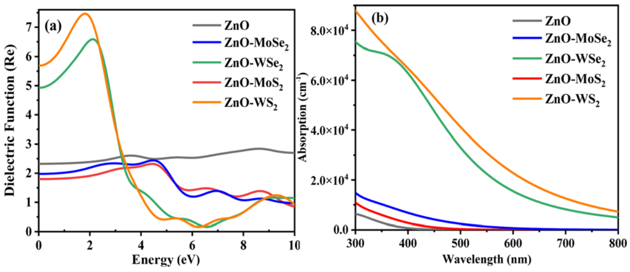

Fig. 6 Optical property spectra of ZnO-based heterojunctions: (a) real part of the dielectric function; (b) absorption spectrum.

Among them, the absorption peaks of ZnO–WS$_2$ and ZnO–WSe$_2$ are significantly higher than those of ZnO–MoS$_2$ and ZnO–MoSe$_2$, indicating that the former two have higher light absorption intensities. The energy range corresponding to visible light is 1.61 to 3.10 eV. Within this range, ZnO–WS$_2$ and ZnO–WSe$_2$ exhibit the best light absorption performance, especially the ZnO–WSe$_2$, which has the highest light absorption rate. Corresponding to Fig. 6(a), the light absorption effect of ZnO–WS$_2$ and ZnO–WSe$_2$ is significantly better than that of ZnO–MoS$_2$ and ZnO–MoSe$_2$.

3.4 Photocatalytic performance

The position of the band edge is one of the core elements for evaluating the performance of a photocatalyst. An ideal photocatalyst should have a band gap that covers the redox potential of water, meaning that the conduction band minimum of the material should be lower than the reduction potential of H$^+$/H$_2$, while the valence band maximum should be higher than the oxidation potential of O$_2$/H$_2$O.[36] This requirement is crucial for the design and selection of efficient photocatalysts, as it not only directly affects the efficiency of photocatalytic water splitting but also determines the stability and service life of the photocatalyst. Based on the concept of semiconductor electronegativity, this paper calculates the oxidation–reduction potential of each system relative to water, with the specific expression given in ref. 37.

$$E_{\mathrm{VBM}} = \chi - E_{\mathrm{elec}} + 0.5E_{\mathrm{g}} \tag{6}$$

$$E_{\mathrm{CBM}} = E_{\mathrm{VBM}} - E_{\mathrm{g}} \tag{7}$$

χ represents the average electronegativity of the atoms in the system, E_{elec} represents a constant value relative to the H electrode ($E_{\mathrm{elec}} = 4.5$ eV), and E_{g} is the band gap of the system. The E_{CBM} and E_{VBM} denote the potential values of the CBM and VBM for ZnO–MX$_2$, as listed in Table 3. Fig. 7 shows the oxidation–reduction band edge positions of ZnO monolayer and four groups of ZnO–MX$_2$.

As shown in Fig. 7, after constructing ZnO-based heterojunctions, their band gaps are significantly reduced and become closer to the redox potential of water, indicating that

Table 3 Shows the CBM and VBM of ZnO–MX$_2$

Heterojunction	ZnO–MoSe$_2$	ZnO–WSe$_2$	ZnO–MoS$_2$	ZnO–WS$_2$
E_{CBM} (eV)	−0.214	−0.165	0.7532	−0.051
E_{VBM} (eV)	2.169	2.263	1.7671	1.442

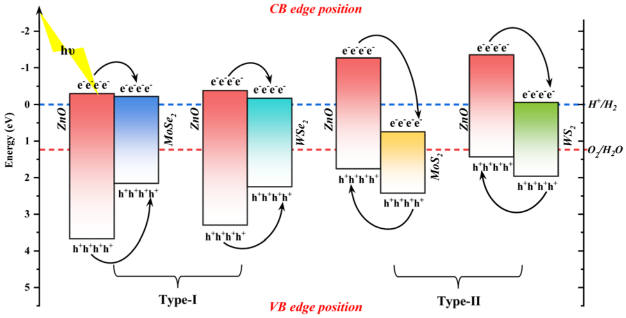

Fig. 7 Shows the oxidation–reduction band edge positions of ZnO monolayer and ZnO–MX_2 heterojunctions (under the condition of pH = 0, with the oxidation–reduction potential of H^+/H_2 and O_2/H_2O).

constructing ZnO-based heterojunctions is an effective strategy to enhance their photocatalytic performance.[38]

Comparing the two types of type-I heterojunctions, ZnO–$MoSe_2$ and ZnO–WSe_2, although their CBMs are both higher than the reduction potential and their VBMs are both lower than the oxidation potential, meeting the basic conditions for redox reactions to occur, it is observed that both electrons and holes mainly migrate from the ZnO layer to the $MoSe_2$ or WSe_2 layers, resulting in difficulty in achieving effective separation of charge carriers. Therefore, such structures are not well-suited to serve as efficient photocatalysts.

It is observed in the two types of type-II heterojunctions, ZnO–MoS_2 and ZnO–WS_2, that both exhibit alternating band structures. Specifically, electrons accumulate in the MoS_2/WS_2 layer, while holes accumulate in the ZnO layer. This electron transfer mechanism helps achieve effective separation of electron–hole pairs, thereby promoting more electrons to participate in redox reactions and significantly enhancing photocatalytic performance.[39,40]

In the ZnO–MoS_2, the CBM of MoS_2 is located below the H^+/H_2 reduction potential, thereby rendering the photocatalyst incapable of hydrogen production. The VBM of ZnO–MoS_2 lies above the O_2/H_2O oxidation potential, thereby enabling the ZnO–MoS_2 system to satisfy the requirements for the oxygen evolution reaction. On the contrary, in ZnO–WS_2, the CBM and VBM are respectively located on the upper and lower sides of the redox potential. Thus, it can be concluded that ZnO–WS_2, as a photocatalyst, is capable of facilitating both HER and OER.

4. Conclusion

The ZnO–MX_2 (M = Mo, W; X = S, Se) heterojunctions exhibit excellent structural stability. The AIMD simulation results show that they have the smallest energy fluctuation amplitude at 300 K. Specifically, the band gaps of ZnO–$MoSe_2$ (1.956 eV), ZnO–WSe_2 (2.098 eV), ZnO–MoS_2 (1.014 eV) and ZnO–WS_2 (1.493 eV) are significantly smaller than that of single-layer ZnO, enabling them to effectively absorb visible light. The electron transfer from MX_2 to ZnO constructs an internal electric field pointing to MX_2 at the interface, further enhancing the charge separation efficiency. ZnO–MS_2 systems form type-II heterojunctions, whereas ZnO–MSe_2 systems form type-I heterojunctions. The D values of ZnO–MS_2 are larger than those of ZnO–MSe_2, indicating that the separation of electrons and holes in ZnO–MS_2 is more pronounced. This reduces the likelihood of recombination and facilitates the further separation of photogenerated carriers. This conclusion aligns with the characteristic of ZnO–MS_2 forming a type-II heterojunction, which enhances the separation of electron–hole pairs.

The static dielectric constants of ZnO–MS_2 systems are greater than that of ZnO–MSe_2 systems, indicating that ZnO–MS_2 systems have better internal field polarization ability, which is highly conducive to the separation of electron–hole pairs. All four heterojunctions exhibit a distinct redshift in the absorption spectrum, among which the absorption coefficient of ZnO–MS_2 systems is greater than that of ZnO–MSe_2 systems.

It can be inferred from the analysis that type-I heterojunctions (ZnO–$MoSe_2/WSe_2$) exhibit inefficient charge separation. In contrast, type-II heterojunctions demonstrate enhanced functionality, as ZnO–MoS_2 promotes oxygen evolution but not hydrogen evolution. Moreover, the bandgap of ZnO–WS_2 straddles the water's redox potentials, indicating that ZnO–WS_2 effectively promotes both OER and HER.

Overall, ZnO–WS_2 emerges as the most promising photocatalyst due to its optimal charge separation, exceptional light absorption, and superior dielectric properties. This work provides critical insights for designing high-performance ZnO-based heterostructures through bandgap engineering and interfacial charge regulation.

Data availability

This study did not generate any new datasets. All data analyzed are from publicly available sources, as cited in the manuscript.

Conflicts of interest

The authors declare that they have no known competing financial interests or personal relationships that could have potentially influenced the work reported in this paper.

Acknowledgements

This study was supported by Xinjiang Yili Normal University Discipline Comprehensive Strength Enhancement Special Project (22XKZZ24); and Science and Technology Project of Xinjiang Yili Kazak Autonomous Prefecture (YZ2022B021).

References

1 D. Zheng, Y. Xue, J. Wang, P. S. Varbanov, J. J. Klemeš and C. Yin, Nanocatalysts in photocatalytic water splitting for green hydrogen generation: Challenges and opportunities, *J. Cleaner Prod.*, 2023, **414**(33), 137700.
2 Y. Dong, Y. Zhang and S. Liu, The impacts and instruments of energy transition regulations on environmental pollution, *Environ. Impact Assess. Rev.*, 2024, **105**(2), 107448.

3 P. Zhou, I. A. Navid, Y. Ma, Y. Xiao, P. Wang, Z. Ye, B. Zhou, K. Sun and Z. Mi, Solar-to-hydrogen efficiency of more than 9% in photocatalytic water splitting, *Nature*, 2023, **613**(7942), 66–70.

4 A. S. Shuaibu, H. Y. Hafeez, J. Mohammed, U. M. Dankawu, C. E. Ndikilar and A. B. Suleiman, Progress on g-C_3N_4 based heterojunction photocatalyst for H_2 production via Photocatalytic water splitting, *J. Alloys Compd.*, 2024, **1002**(33), 175062.

5 J. Fu, K. Jiang, X. Qiu, J. Yu and M. Liu, Product selectivity of photocatalytic CO_2 reduction reactions, *Mater. Today*, 2020, **32**(1), 222–243.

6 X. Zhang, S. Zhang, K. Mathivanan, R. Zhang, J. Zhang, Q. Jiang, W. Sand, J. Duan and B. Hou, Research progress and prospects in antifouling performance of photocatalytic sterilization: A review, *J. Mater. Sci. Technol.*, 2025, **208**(5), 189–201.

7 I. Ahmad, Y. Zou, J. Yan, Y. Liu, S. Shukrullah, M. Y. Naz, H. Hussain, W. Q. Khan and N. R. Khalid, Semiconductor photocatalysts: A critical review highlighting the various strategies to boost the photocatalytic performances for diverse applications, *Adv. Colloid Interface Sci.*, 2023, **311**(1), 102830.

8 Y. Ying, K. Fan, Z. Lin and H. Huang, Facing the "Cutting Edge:" Edge Site Engineering on 2D Materials for Electrocatalysis and Photocatalysis, *Adv. Mater.*, 2025, **37**(10), 2418757.

9 Y. Tang, Y. Lu, B. Ma, J. Song, L. Bai, Y. Wang, Y. Chen and M. Liu, Rational Design of ZnO/Sc_2CF_2 Heterostructure with Tunable Electronic Structure for Water Splitting: A First-Principles Study, *Molecules*, 2024, **29**(19), 4638.

10 P. Dhiman, G. Rana, A. Kumar, G. Sharma, D.-V. N. Vo and Mu. Naushad, ZnO-based heterostructures as photocatalysts for hydrogen generation and depollution: a review, *Environ. Chem. Lett.*, 2022, **20**(2), 1047–1081.

11 G. Wang, H. Yuan, J. Chang, B. Wang, A. Kuang and H. Chen, One-step in-situ construction engineering of ZnO-Zn_2SnO_4 heterojunction for deeply photocatalytic oxidation of nitric oxide, *J. Colloid Interface Sci.*, 2024, **664**(12), 433–443.

12 R. Yang, Y. Fan, Y. Zhang, L. Mei, R. Zhu, J. Qin, J. Hu, Z. Chen, Y. Hau Ng, D. Voiry, *et al*, 2D Transition Metal Dichalcogenides for Photocatalysis, *Angew. Chem., Int. Ed.*, 2023, **62**(13), e202218016.

13 J. Tao, L. Huang, S. Xiong, L.-X. Li, L.-L. Wang and L. Xu, Two-dimensional TMDs/MN (M = Al, Ga) van der Waals heterojunction photocatalyst: a first-principles study, *J. Mater. Sci.*, 2023, **58**(35), 14080–14095.

14 Y. Jin, M. Jin, J. Bai, J. Li, Z. Wu, Z. Li, J. Xiang and C. Guo, Mechanism analysis of photocatalytic activity on Semiconductor-Type-Modulated heterojunctions, *Appl. Surf. Sci.*, 2024, **656**(15), 159683.

15 M. Haddad, A. Belhadi, L. Boudjellal and M. Trari, Photocatalytic hydrogen production on the hetero-junction CuO/ZnO, *Int. J. Hydrogen Energy*, 2021, **46**(75), 37556–37563.

16 H. Li, R. Wu, J. Ji, Y. Liu, J. Zhao, S. Sahar and A. Zeb, Efficient CeO_2/ZnO heterojunction for enhanced heterogeneous photocatalytic application, *Inorg. Chem. Commun.*, 2025, **171**(1), 113553.

17 X. Yuan, M. Wu, J. Ni, Y. Cheng and C. Ni, Tuning the ZnO/GaN heterojunction for atmospheric NO abatement, *Appl. Surf. Sci.*, 2023, **635**(29), 157712.

18 G. Jia, Y. Zhang and P. Wang, Nano-photo-thermal energy drive MoS_2/ZnO nanoheterojunctions growing, *Opt. Mater. Express*, 2016, **6**(3), 876–883.

19 G. Jiang, C. Yao, Z. Wang, X. Wang and Y. Cai, Semiconducting ZnO & WS_2 heterojunction composite films: Fabrication, characterization and ultrafast nonlinear properties, *J. Alloys Compd.*, 2021, **863**(14), 158664.

20 Y. Guan and Y. Du, Two-dimensional ZnO/$MoSe_2$ van der Waals heterostructure used as promising photocatalyst for water splitting: A DFT study, *Chem. Phys. Lett.*, 2022, **803**(18), 139828.

21 G. Wang, H. Yuan, J. Chang, B. Wang, A. Kuang and H. Chen, ZnO/MoX_2 (X = S, Se) composites used for visible light photocatalysis, *RSC Adv.*, 2018, **8**(20), 10828–10835.

22 A. S. Oreshonkov, Electronic transitions and vibrational properties of bulk and monolayer g-C_3N_4, and a g-C_3N_4/MoS_2 heterostructure from a DFT study, *Phys. Chem. Chem. Phys.*, 2024, **26**(35), 23023–23031.

23 X. Zhang, 1 D CeO_2/g-C_3N_4 type II heterojunction for visible-light-driven photocatalytic hydrogen evolution, *Inorg. Chem. Commun.*, 2022, **144**(10), 109838.

24 L. Luan, L. Han, D. Zhang, K. Bai, K. Sun, C. Xu, L. Li and L. Duan, AlSb/ZrS_2 heterojunction: A direct Z-scheme photocatalyst with high solar to hydrogen conversion efficiency and catalytic activity across entire PH range, *Int. J. Hydrogen Energy*, 2024, **51**(3), 1242–1255.

25 Z.-L. Liu, R.-R. Liu, Y.-F. Mu, Y.-X. Feng, G.-X. Dong, M. Zhang and T.-B. Lu, In Situ Construction of Lead-Free Perovskite Direct Z-Scheme Heterojunction $Cs_3Bi_2I_9$/Bi_2WO_6 for Efficient Photocatalysis of CO_2 Reduction, *Sol. RRL*, 2021, **5**(3), 2000691.

26 Y. Zhang, Z. Qiang, J. Ding, K. Xie, L. Duan and L. Ni, First-principles prediction of a direct Z-scheme WSe_2/HfS_2 van der Waals heterostructure for overall photocatalytic water decomposition, *CrystEngComm*, 2024, **26**(60), 2621–2634.

27 Y. Zhang, W. Yang, Z. Zhu, L. Zhang and W. Peng, Temperature-Sensitive Template for Preparation of ZnO/CeO_2 Composite Photocatalytic Materials and Its Catalytic Performance, *Molecules*, 2024, **29**(15), 3589.

28 J. Wang, Y. Sun, J. Lai, R. Pan, Y. Fan, X. Wu, M. Ou, Y. Zhu, L. Fu, F. Shi and Y. Wu, Two-dimensional graphitic carbon nitride/N-doped carbon with a direct Z-scheme heterojunction for photocatalytic generation of hydrogen, *Nanoscale Adv.*, 2021, **3**(23), 6580–6586.

29 K. Tian, G. Qian, Q. Liu, X. Fu, S. Zhang, Q. Xie and X. Luo, Direct Z-scheme GeC/GaSe heterojunction by first-principles study for photocatalytic water splitting, *Mater. Sci. Semicond. Process.*, 2024, **184**(16), 108855.

30 Y. Liu, Y. Yao, Z. Liang, Z. Gong, J. Li, Z. Tang and X. Wei, Two-Dimensional AlN/PtSSe Heterojunction as A Direct Z-Scheme Photocatalyst for Overall Water Splitting: A DFT Study, *J. Phys. Chem. C*, 2024, **128**(24), 9894–9903.

31 N. Jaykhedkar, R. Bystrický, M. Sýkora and T. Bučko, How the Temperature and Composition Govern the Structure and Band Gap of Zr-Based Chalcogenide Perovskites: Insights from ML Accelerated AIMD, *Inorg. Chem.*, 2023, **62**(31), 12480–12492.

32 C. Zhao, Z. Li and Z. Zhang, Stable WSeTe/PtTe$_2$ van der Waals heterojunction: Excellent mechanical, electronic, and optical properties and device applications, *Appl. Surf. Sci.*, 2024, **672**(31), 160859.

33 K. Si, J. Ma, C. Lu, Y. Zhou, C. He, D. Yang, X. Wang and X. Xu, A two-dimensional MoS$_2$/WSe$_2$ van der Waals heterostructure for enhanced photoelectric performance, *Appl. Surf. Sci.*, 2020, **507**(9), 145082.

34 I. Ahmad, S. Shukrullah, M. Yasin Naz, S. Ullah and M. Ali Assiri, Designing and modification of bismuth oxyhalides BiOX (X = Cl, Br and I) photocatalysts for improved photocatalytic performance, *J. Ind. Eng. Chem.*, 2022, **105**(1), 1–33.

35 F. Hu, L. Tao, H. Ye, X. Li and X. Chen, ZnO/WSe$_2$ vdW heterostructure for photocatalytic water splitting, *J. Mater. Chem. C*, 2019, **7**(23), 7104–7113.

36 A. Bao, Y. Ma, X. Guo, J. Wang, Y. Zhao, Z. Liu, Y. Wang, X. Liu and Y. Zhang, Tunable electronic and optical properties of a type-II GaP/SiH van der Waals heterostructure as photocatalyst: A first-principles study, *Int. J. Hydrogen Energy*, 2024, **88**(28), 1256–1266.

37 Z.-N. Dai, Y. Xu, D. F. Zou, W. J. Yin and J. N. Wang, InN/XS$_2$ (X = Zr, Hf) vdW heterojunctions: promising Z-scheme systems with high hydrogen evolution activity for photocatalytic water splitting, *Phys. Chem. Chem. Phys.*, 2023, **25**(11), 8144–8152.

38 I. Ahmad, R. Bousbih, A. Mahal, W. Q. Khan, M. Aljohani, M. A. Amin, N. N. A. Jafar, M. S. Jabir, H. Majdi, A. S. Alshomrany, M. Shaban, I. Ali and H. Bayahia, Recent progress in ZnO-based heterostructured photocatalysts: A review, *Mater. Sci. Semicond. Process.*, 2024, **180**(12), 108578.

39 Q. Fan, Z. Yan, J. Li, X. Xiong, K. Li, G. Dai, Y. Jin and C. Wu, Interfacial-electric-field guiding design of a Type I FeIn$_2$S$_4$@ZnIn$_2$S$_4$ heterojunction with ohmic-like charge transfer mechanism for highly efficient solar H$_2$ evolution, *Appl. Surf. Sci.*, 2024, **663**(22), 160206.

40 X. T. Zhu, Y. Xu, Y. Cao, Y. Q. Zhao, W. Sheng, G.-Z. Nie and Z. Ao, Investigation of the electronic structure of two-dimensional GaN/Zr$_2$CO$_2$ hetero-junction: Type-II band alignment with tunable band gap, *Appl. Surf. Sci.*, 2021, **542**(8), 148505.